JOURNAL OF COMPUTATIONAL PHYSICS 37, 151–170 (1980)

# Computer Simulation of Trapped-Electron Modes in Tokamaks

T. L. CRYSTAL AND J. DENAVIT

*Department of Mechanical and Nuclear Engineering*
*Northwestern University, Evanston, Illinois 60201*

Received April 26, 1979; revised August 22, 1979

This paper presents a numerical method for solving in time the linearized drift-kinetic equation in toroidal geometry, in the local approximation; collisions are represented using a Lorentz model for pitch-angle diffusion. This method is applicable to computer simulations of dissipative trapped-electron modes in tokamaks, including the effects of magnetic curvature and gradient drifts. The accuracy, convergence, and numerical stability of the method are analyzed, and the results of computations verifying these analyses are given.

## I. INTRODUCTION

The non-uniformity of the magnetic field along the lines of force in toroidal confinement devices, such as tokamaks, is responsible for particle trapping and associated low-frequency instabilities [1, 2], which have been the object of recent theoretical studies because of their expected effect on plasma density fluctuations [3]. We present in this paper a computer simulation method for trapped-electron modes, based on numerical solution of the drift-kinetic equation in toroidal geometry.

Before entering into the discussion of these numerical solutions, a brief review of physical concepts related to trapped-electron modes is given to introduce the notations and to define the physical scope of the simulations. Trapped particles occur in toroidal devices because the magnetic field intensity along a given line of force has minima, $B_{\min}$, at $\theta = 0$ and maxima, $B_{\max}$, at $\theta = \pi$, where $\theta$ denotes the poloidal angle (Fig. 1a), $B_{\min}/B_{\max} \simeq 1 - 2\varepsilon$, and $\varepsilon = r/R_0 \ll 1$ is the flux surface inverse aspect ratio. Particles at $\theta = 0$ with pitch angle $\alpha$ satisfying the relation $|\cos\alpha| < (2\varepsilon)^{1/2}$ are reflected before reaching a field maximum at $\theta = \pi$. Such particles are in this way trapped in the outer region of the toroidal flux surface and oscillate about $\theta = 0$ with a "bounce" frequence $\omega_b \simeq \gamma v \varepsilon^{1/2}/r$, where $v$ is the speed of the particle (Fig. 1b) and $\gamma$ is the angle of the magnetic field **B** with respect to the $\zeta$ direction (Fig. 1c). Particles with $|\cos\alpha| > (2\varepsilon)^{1/2}$ have sufficiently large parallel velocities to pass through the field maxima at $\theta = \pi$ and therefore circulate, or transit, around the torus.



0021-9991/80/110151-20$02.00/0

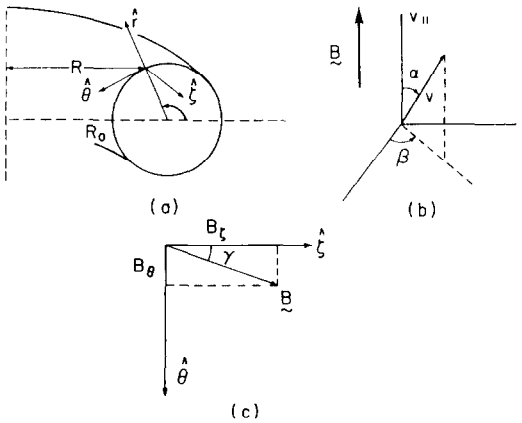


FIG. 1. Geometric relations defining trapped-particle motion in toroidal plasmas.

In analytical treatments of trapped-electron modes, dispersion relations are usually derived by considering trapped and transiting electrons as separate species. The response of transiting (i.e., untrapped) electrons to a low-frequency electric potential $\varphi$ is found approximately from the Boltzmann relation, which gives their density perturbation $\delta n_e^U \simeq N_0 e\varphi/T_e$, where $N_0$ and $T_e$ are the electron density and temperature and $-e$ is the electron charge. Trapped electrons, however, are constrained and therefore cannot reach this equilibrium density. Their distribution function is evaluated by integrating their kinetic equation along unperturbed trapped orbits, and then averaging the resulting density perturbation over a bounce period [1–3].

Electron–ion collisions play an important role in trapped-electron modes in that they can scatter electrons out of the trapped-particle region; they are often introduced in analytical treatments by using a Krook collision operator of the form $(\partial f/\partial t)_{\text{coll}} = -\nu_{\text{ef}}[f - f^0 \exp(e\varphi/T_e)]$ which is applied only to trapped particles. Here, $f^0$ denotes the Maxwellian distribution and $\nu_{\text{ef}} = \nu/\varepsilon$ is an "effective" collision frequency, accounting for the rate of pitch-angle scattering of electrons out of the trapped-particle region. For Coulomb scattering, the collision frequency $\nu_{\text{ef}}$ is also inversely proportional to $v^3$.

The general problem of trapped-particle modes is three-dimensional, involving the poloidal and toroidal angles, $\theta$ and $\zeta$, respectively, on a given flux surface, and the minor radius $r$ of the flux surface. These modes may, however, be studied in the "local approximation" in which the wave vector $\mathbf{k}$ is assumed parallel to a flux surface of minor radius $r$, and the radial dependence enters only through the density and temperature gradients defined by the parameters $L_n^{-1} = -(dN_0/dr)/N_0$ and $\eta = (N_0/T_e)(dT_e/dr)/(dN_0/dr)$.

The numerical solutions considered in this paper are linearized and are done in the local approximation, but they go beyond analytical treatments of the problem in the following important aspects:

(1) No a priori distinction is made between trapped and transiting electrons. The behavior of trapped electrons, including curvature and gradient drifts, follows from the solution of the drift-kinetic equation and does not involve the introduction of approximate bounce-averaged unperturbed orbits. Thus, for example, the motions of marginally trapped electrons having long bounce periods of the order of the wave period are taken into account.

(2) Collisions are included in terms of a Lorentz model $(\partial f/\partial t)_{\text{coll}} = (v/\sin\alpha)(\partial/\partial\alpha)(\sin\alpha\,\partial f/\partial\alpha)$ instead of the Krook model. The Lorentz model accurately accounts for pitch-angle scattering of both trapped and transiting particles, without having to introduce an effective collision frequency which assumes that the trapped particles' pitch-angle distribution remains constant with time.

(3) The electric potential is computed from Poisson's equation, instead of assuming charge neutrality. This introduces the Debye length, $\lambda_D$, into the computations and causes the appearance of high-frequency oscillations at the frequency $\omega_h = \omega_e k_\parallel/k$ as the system seeks to establish charge neutrality. Here $\omega_e = v_e/\lambda_D$ is the plasma frequency, $v_e = (T_e/m_e)^{1/2}$ is the electron thermal velocity and $k_\parallel$ is the wave vector component parallel to **B**.

In the local approximation, the drift-kinetic equation involves four dimensions, in addition to time: two spatial variables, the poloidal and toroidal angles $\theta$ and $\zeta$ (Fig. 1a), and two velocity variables, the electron speed $v$ and pitch angle $\alpha$ (Fig. 1b). As in the case of the Vlasov equation, the drift-kinetic equation may be solved numerically either directly, or after transformation with respect to some of these variables. Here, Fourier transforms are taken with respect to $\theta$ and $\zeta$, but the solution is carried out directly with respect to $v$ and $\alpha$, or to be exact, with respect to $v$ and $u = \cos\alpha$. Since the solutions are linearized, and the equilibrium distribution function is independent of $\zeta$, only a single toroidal mode need be considered, thus effectively reducing the dimensionality from 4 to 3. On the other hand, the $\theta$-dependence of the magnetic field results in electron trapping and this appears in the electrons' transformed drift-kinetic equation as poloidal mode coupling; thus several poloidal modes need to be considered simultaneously. However, we show in this paper that the number of these poloidal modes required to recover trapping effects is small, varying from three to nine, depending on the trapping phenomenon being considered. Using the velocity variables $v$ and $u$ directly allows an accurate representation of resonant particle effects.

The equations forming the basis of the present simulation method are given in Section II. The algorithm to advance the potential and the electron distribution function is presented in Section III. Here, a form of split time-step algorithm is introduced: the distribution function is advanced in a collisionless manner during the first half time-step, which requires an iteration process, and the Lorentz collision term is applied in the second half time-step. This method has certain advantages in both simplicity and accuracy as discussed in part (1) of Section IV. In these solutions, both low- and high-frequency oscillations occur simultaneously. Although the low-frequency oscillations are of primary physical interest, it is the high-frequency oscillations which dominate the convergence and numerical stability of the solution.

After gaining some experience with the computations, it was recognized that the numerical stability depends in this case on the *parity* of the number of iterations. This question is analyzed in parts (2) and (3) of Section IV, where the growth rate of the numerical instability is derived. The several examples of this algorithm and its stability tests presented in Section V include: (1) unperturbed trapped-electron behavior; (2) drift wave simulations, showing resonant damping and growth; (3) examples of high-frequency oscillations relating to the numerical stability of this simulation approach; and (4) a series of simulations of the curvature and gradient drift resonance instability to establish the number of poloidal modes required to obtain accurate results in the simulation of trapped-electron modes. In the Appendix, we show that, with the ion model used here, the approximation of charge neutrality would not eliminate the troublesome high-frequency oscillations and in fact would have the opposite effect, making their frequency even higher.

## II. Basic Equations

The magnetic field geometry of a toroidal tokamak device is approximated by using a curvilinear coordinate system, $\mathbf{x} = (r, \theta, \zeta)$, which is defined by a nested set of toroidal flux surfaces of major radius $R_0$, having circular cross sections with minor radii $r$, as shown in Fig. 1a. Drift waves in this device are analyzed here in the local approximation, where the wave vector $\mathbf{k}$ is restricted to lie in a chosen flux surface and the wave electric field is expressed as $\mathbf{E} = -(\partial\varphi/\partial\theta)(\hat{\theta}/r) - (\partial\varphi/\partial\zeta)(\hat{\zeta}/R)$, where $\varphi$ is the electron potential, $\theta$ and $\zeta$ are the poloidal and toroidal angles, respectively, and $R = R_0(1 + \varepsilon \cos\theta)$.

Electrons are described using their distribution function $F(v, \alpha, \mathbf{x}, t)$, averaged over Larmor phase $\beta$ and dependent on velocity through the electron speed, $v$, and pitch angle, $\alpha$, defined in Fig. 1b. This distribution function evolves in time according to the drift-kinetic equation [4]. In the solutions considered here, the drift-kinetic equation is linearized by setting $F = f^{eq} + f$, where $f^{eq}$ denotes the equilibrium distribution function, and $f$ is the perturbation associated with the waves.

The equilibrium distribution function is [5, 6]

$$f^{eq} = \left\{1 + \frac{v\cos\alpha}{\gamma\Omega_e L_n}\left[1 + \frac{\eta}{2}\left(\frac{m_e v^2}{T_e} - 3\right)\right]\right\} f^0,$$

where

$$f^0 = N_0\left(\frac{m_e}{2\pi T_e}\right)^{3/2} \exp\left(-\frac{m_e v^2}{2T_e}\right),$$

$\Omega_e = eB/m_e c$ is the electron cyclotron frequency, $m_e$ is the electron mass and $c$ is the speed of light.

The perturbation distribution function is represented through its Fourier transform with respect to the poloidal and toroidal angles, defined by

$$f_{m+l}=\frac{1}{4\pi^2}\int_0^{2\pi}d\theta\int_0^{2\pi}d\zeta f(\theta,\zeta)\exp\{-i[(m+l)\,\theta+n\zeta]\},$$

and the Fourier transform $\varphi_{m+l}$ of the potential is defined in similar manner. After linearization and Fourier transformation, the electron drift-kinetic equation yields [5, 6]

$$\begin{aligned}\frac{\partial f_{m+l}}{\partial t}=\nu(v)\frac{\partial}{\partial u}\left[(1-u^2)\frac{\partial f_{m+l}}{\partial u}\right]-iuv(k_\parallel+l)(f_{m+l}-f^0\varphi_{m+l})\\ -i\frac{v_D}{\gamma}\left[1+\frac{\eta}{2}(v^2-3)\right](m-k_\parallel)f^0\varphi_{m+l}\\ +i\frac{\varepsilon v(1-u^2)}{4}\frac{\partial}{\partial u}(f_{m+l+1}-f_{m+l-1})\\ -i\frac{v^2(1+u^2)}{4\gamma}\varepsilon\frac{\rho_e}{r}[(m+l+1)(f_{m+l+1}-f^0\varphi_{m+l+1})\\ +(m+l-1)(f_{m+m-1}-f^0\varphi_{m+l-1})],\end{aligned}\tag{1}$$

where $v_D=T_e/m_e\Omega_eL_n$ is the electron diamagnetic drift velocity. As indicated earlier, mode coupling occurs only between the poloidal modes; therefore a spectrum of poloidal modes with a central mode $m$ and several satellites defined by $l=0,\pm1,...,\pm l_{max}$ must be considered. On the other hand a single toroidal mode, $n$, is sufficient. In Eq. (1), all quantities have been normalized with lengths measured in units of $r/\gamma$ (distance travelled by electrons per radian around the minor axis), velocities in units of the electron thermal velocity $v_e$, times in units of $r/\gamma v_e$, potential in units of $T_e/e$ and density in units of $N_0$. Also defined here are $u=\cos\alpha$ and $\rho_e=v_e/\Omega_e$, mean (thermal) electron gyroradius.

A derivation of Eq. (1) which assumes $\varepsilon\ll1$, $\gamma\ll1$ and $\rho_e/r\ll1$ is presented elsewhere [6], but its terms may be identified as follows. The first term in the right member is the collision term, chosen according to the Lorentz model, which gives a collisional diffusion in pitch angle $\alpha$. The collision frequency defined by $\nu=\nu_0(2/(1+v^2))^{3/2}$, is a function of energy approaching the $v^{-3}$ dependence of the Coulomb cross section for large $v$. This energy dependence plays an important role in the dissipative trapped-electron instability. The second term accounts for streaming parallel to the magnetic field, where $k_\parallel=m+n\varepsilon/\gamma<1$, is the wave vector component parallel to **B**, corresponding to the central mode $(m, n)$. The third term accounts for electric field effects related to the radial density and temperature gradients. The fourth term, which accounts for trapping of electrons due to magnetic field inhomogeneity, introduces coupling between adjacent poloidal modes. The last term, which also involves mode coupling, represents the effect of curvature and gradient drifts. This term is responsible for a resonance which destabilizes trapped-electron modes in the low-collisionality regime [7].

Assuming cold ions and a wave frequency $\omega \ll \Omega_i$, where $\Omega_i$ is the ion gyrofrequency, the ion velocity reduces to the electric drift velocity and the ion continuity equation gives $\partial N_{i\,m+l}/\partial t \simeq -(imv_D/\gamma)\varphi_{m+l}$, where $N_{i\,m+l}$ is the ion density of poloidal mode $m+l$. The corresponding expression for $\partial N_{e\,m+l}/\partial t$ is obtained by integrating Eq. (1) with respect to velocity. Substituting these expressions into the time derivatives of the Poisson equation yields [5, 6]

$$\frac{d\varphi_{m+l}}{dt} + \frac{ik_\parallel \gamma v_D}{m^2\lambda_D^2}\varphi_{m+l} = \frac{i\gamma^2}{m^2\lambda_D^2}\left\{(k_\parallel + l)\langle v_\perp\rangle_{m+l} - \frac{\varepsilon}{2}(\langle v_\perp\rangle_{m+l+1} - \langle v_\parallel\rangle_{m+l-1}) + \frac{\varepsilon\rho_c}{\gamma r}[(m+l+1)(p_{m+l+1} - \varphi_{m+l+1}) + (m+l-1)(p_{m+l-1} - \varphi_{m+l-1})]\right\}, \tag{2}$$

where $\langle v_\parallel\rangle_m = 2\pi \int uv^3 f_m\, du\, dv$, $p_m = \frac{1}{2}\pi \int (1+u^2)\, v^4 f_m\, du\, dv$ and $\lambda_D$ denotes the Debye length, measured in units of $r/\gamma$.

## III. Algorithm

From the preceding formulation, the drift-kinetic equation, Eq. (1), can be used as the "updater" for the spectral components, $f_{m+l}$, of the electron distribution. Similarly, the Poisson equation, Eq. (2), can be used as the updater for the wave potentials, $\varphi_{m+l}$, after the velocity integrals, $\langle v_\parallel\rangle_{m+l}$ and $p_{m+l}$, have been computed. These equations form a system of coupled equations, whose numerical solution is to be generated.

Each spectral component, $f_{m+l}$, with $l = 0, \pm 1, \ldots, \pm l_{max}$, is represented over a discrete grid in speed and pitch angle $(v_j, u_k)$, as shown in Fig. 2, where $v_j = j\,\Delta v$ and $u_k = k\,\Delta u$ with $j = 0, \ldots, j_{max}$ and $\Delta v = v_{max}/j_{max}$; similarly $k = 0, \pm 1, \ldots, \pm k_{max}$ and $\Delta u = 1/k_{max}$. The derivatives with respect to $u$ are computed by finite differences,

$$\partial f/\partial u|_{u_k} \simeq [f(u_{k+1}) - f(u_{k-1})]/2\Delta u,$$
$$\partial^2 f/\partial u^2|_{u_k} \simeq [f(u_{k+1}) - 2f(u_k) + f(u_{k-1})]/\Delta u^2,$$

and the integrals over $u$ and $v$ are computed using Simpson's rule. At the boundaries $u = \pm 1$, the second-order derivative $\partial^2 f/\partial u^2$ does not enter in Eq. (1) and the first-order derivative, which enters in the collision term, is computed by the non-centered differences $\partial f/\partial u|_{u=\pm 1} = \pm[f_{\pm k_{max}} - f_{\pm(k_{max}-1)}]/\Delta u$. These boundary derivatives are computed as centered derivatives by introducing two columns of guard points corresponding to $k = \pm(k_{max}+1)$ and defining $f_{\pm(k_{max}+1)} = 2f_{\pm k_{max}} - f_{\pm(k_{max}-1)}$.

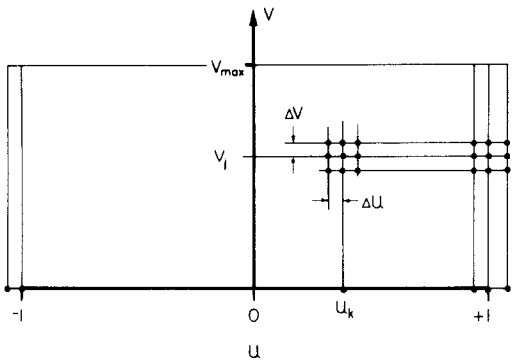


FIG. 2. Grid for representation of electron distribution in speed $v = [0, v_{max}]$ and pitch-angle $u = \cos\alpha = [-1, +1]$ with guard points shown at $u = \pm(1 + \Delta u)$.

Consider the right side of Eq. (1) as being composed of a collisional diffusion term, denoted as $D$, plus a streaming term $-iuv(k_\| + l)f_{m+l}$, plus the remaining terms, denoted as $C$. The time derivative in Eqs. (1) and (2) are replaced with finite differences and the finite time step is made implicit by replacing $f_{m+l}$ and $\varphi_{m+l}$ on the right sides with averages between their new values (at time $t + \Delta t$) denoted with primes, and their known present values (at time $t$) denoted as unprimed. Once in this form, Eq. (1) can be solved for the quantity $f'_{m+l}$ as it appears in the derivative and streaming term:

$$f'_{m+l} = (1 + iuv(k_\| + l)\,\Delta t/2)^{-1}\left\{(1 - iuv(k_\| + l)\,\Delta t/2)f_{m+l} + \frac{\Delta t}{2}(C + D) + \frac{\Delta t}{2}(C' + D')\right\}. \tag{3}$$

A similar expression is obtained from Eq. (2) for the potentials $\varphi'_{m+l}$.

In the first algorithm considered for these simulations, all the right-side terms of Eq. (3) are used to advance $f_{m+l}$ in a single iterated time step as shown schematically in Fig. 3a. The iterations are carried out on the terms $C' + D'$ in Eq. (3) and on the corresponding terms in the equation for $\varphi'_{m+l}$.

The difficulty with this first algorithm is that the time step size $\Delta t$ is limited by the collision frequency and the interval $\Delta u$. Convergence problems arise whenever $\nu\,\Delta t/\Delta u^2 \gtrsim 1$. This limitation could be overcome by moving the term $D'$ to the left side of Eq. (3) and solving the resulting tridiagonal matrix at each iteration. However, the tridiagonal matrix would comprise complex elements and would not permit vectorization of the code.

These complications are avoided by implementing a second algorithm using a split time step as shown schematically in Fig. 3b. Here the iterated first half-step is

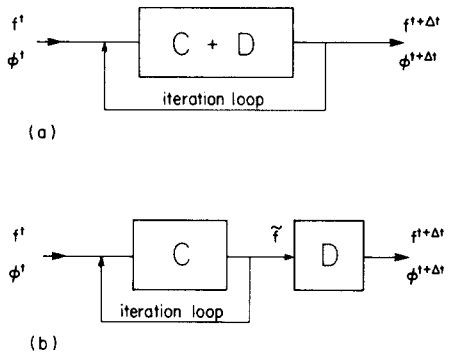


FIG. 3. The two iterated time-stepping schemes: (a) single step; (b) split step, with tridiagonal diffusion matrix outside of iteration loop.

collisionless, solving Eq. (3) with $D = D' = 0$ to obviate the above mentioned limit on $\Delta t$. The second half-step applies a pure diffusion operator

$$f'_{m+1} - \frac{D' \Delta t}{2} = \frac{\tilde{D} \Delta t}{2} \tag{4}$$

for the collisions, which is solved exactly by inverting what is now a real tridiagonal matrix. With the diffusion term removed from the iteration loop, the first half-step can now be vectorized.

This split-step algorithm is not only significantly more efficient to run, the analysis given in Section IV will show that in the case $\nu \ll \omega$, its accuracy is also superior to that of the single-step algorithm.

## IV. ACCURACY, CONVERGENCE, AND STABILITY

In the present algorithm, the Poisson equation (actually, its time derivative Eq. (2)) is used to compute the wave fields: no charge neutrality condition is imposed. With electrons flowing parallel to **B** in response to electric fields having a wave vector component $k_\parallel$ parallel to **B**, electron oscillations occur at the frequency $\omega_h = \omega_e k_\parallel / k$, where $\omega_e = v_e / \lambda_D$ is the electron plasma frequency and $k$ is the wave vector magnitude. This high-frequency oscillation is superimposed over the low-frequency drift wave at frequency $\omega_* = k_\perp v_D$, where $k_\perp$ is the wave vector component perpendicular to **B**. Although the drift wave is of primary interest in the present computations, it is the high-frequency oscillations which cause the time-step limitations (related to accuracy, convergence, and numerical stability questions) which will be considered in this section.

To analyze the high-frequency behavior of the code, we can neglect terms related to diamagnetic drift and trapping by setting $v_D = 0$, $\rho_e / r = 0$, and $\varepsilon = 0$, and consider

a single poloidal mode (there is no electron trapping when $\varepsilon = 0$ and therefore no mode coupling occurs). It will also be sufficient for our purposes in this section to consider a monoenergetic distribution, $f^0 = \delta(v-1)/4\pi$, so that $f_{m+l}$ reduces to a function of $u$ and $t$ only, and Eqs. (1) and (2) reduce to

$$\frac{\partial f}{\partial t} = v\frac{\partial}{\partial u}\left[(1-u^2)\frac{\partial f}{\partial u}\right] - iuvk_l(f-\varphi), \tag{5}$$

$$\frac{\partial \varphi}{\partial t} = i\frac{\gamma^2 k_l}{2m^2\lambda_D^2}\int_{-1}^{+1} uf\,du, \tag{6}$$

where the subscripts $m+l$ have been omitted from $f$ and $\varphi$, and $k_l = k_\parallel + l$ is the parallel wave vector component of the mode considered.

To obtain an analytical solution of Eqs. (5) and (6), the pitch-angle dependence of $f$ is expanded as $f = \sum_j F_j P_j(u)$, where $P_j(u)$ denotes the Legendre polynomial of order $j$, and the $F_j(t)$ are the associated time-dependent coefficients. After truncating the expansion for $j \geqslant 2$, Eqs. (5) and (6) yield

$$\dot{F}_0 = -(ik_l/3)F_1, \tag{7}$$

$$\dot{F}_1 = -ik_l(F_0 - \varphi) - 2vF_1, \tag{8}$$

$$\dot{\varphi} = i\frac{k_l\gamma^2}{m^2\lambda_D^2}\langle v_\parallel\rangle = i\frac{\omega_h^2}{k_l}F_1, \tag{9}$$

where $\langle v_\parallel\rangle = \frac{1}{2}\int_{-1}^{+1} uf\,du$ and $\omega_h = \gamma k_l/3^{1/2}m\lambda_D$ for this monoenergetic case. Assuming a time dependence of the form $\exp(-i\omega t)$, these equations yield the dispersion relation

$$\omega^2 + 2iv\omega - \omega_0^2 = 0, \tag{10}$$

where $\omega_0^2 = \omega_h^2 + k_l^2/3$. Solving Eq. (10) for complex frequency $\omega$, it follows that the fields oscillate at the frequency $\beta = \mathrm{Re}(\omega) = (\omega_0^2 - v^2)^{1/2}$ and are collisionally damped at the rate $\Gamma = \mathrm{Im}(\omega) = -v$. Because of the truncation of the Legendre polynomials for $j \geqslant 2$, we do not recover Landau damping in the present analysis.

We now compare these values of $\beta$ and $\Gamma$ with the values obtained from the finite-difference solutions to Eqs. (7) through (9) using first the single-step and later the split-step algorithms.

1. *Accuracy of Single-step Algorithm*

Denoting new quantities (at time $t + \Delta t$) with primed variables and old quantities (at time $t$) with unprimed variables, Eqs. (7) through (9) yield in this case (see Fig. 3a),

$$F_0' - F_0 = -ik_l\Delta t(F_1' + F_1)/6, \tag{11}$$

$$F_1' - F_1 = -ik_l\Delta t(F_0' + F_0 - \varphi' - \varphi)/2 - v\Delta t(F_1' + F_1), \tag{12}$$

$$\varphi' - \varphi = i\frac{\omega_h^2\Delta t}{2k_l}(F_1' + F_1). \tag{13}$$

Assuming complete convergence of the iteration and a time dependence of the form $\exp(-i\omega t)$ yields the dispersion relation

$$z^2 + 2ivz - \omega_0^2 = 0, \tag{14}$$

which is identical to Eq. (10), except that for $\omega$ we now have $z$, where

$$z = \frac{2}{\Delta t}\tan\left(\frac{\omega\,\Delta t}{2}\right) = \omega\left(1 + \frac{\omega^2\,\Delta t^2}{12} + \frac{\omega^4\,\Delta t^4}{120} + \cdots\right). \tag{15}$$

Solving Eqs. (14) and (15) for $\beta_1 = \mathrm{Re}(\omega)$ and $\Gamma_1 = \mathrm{Im}(\omega)$ and comparing with the earlier values of $\beta$ and $\Gamma$ yields the relative frequency and growth rate errors,

$$\frac{\beta_1 - \beta}{\beta} = -\frac{\omega_0^2 - 4v^2}{12}\Delta t^2 - \frac{(\omega_0^2 - v^2)^2}{120}\Delta t^4 + O(\Delta t^6), \tag{16}$$

$$\frac{\Gamma_1 - \Gamma}{\Gamma} = \frac{-3\omega_0^2 + 4v^2}{12}\Delta t^2 - \frac{(\omega_0^2 - v^2)^2}{24}\Delta t^4 + O(\Delta t^6). \tag{17}$$

2. *Accuracy of Split-Step Algorithm*

In this algorithm, the collision term is outside the iteration loop and solved separately, as shown in Fig. 3b. Denoting the intermediate value of $F_1$ with a tilde, and noting that collisional diffusion does not affect $\varphi$, Eq. (12) should be replaced by

$$\tilde{F}_1 - F_1 = -ik_l\,\Delta t(F_0' + F_0 - \varphi' - \varphi)/2, \tag{18}$$

$$F_1' - \tilde{F}_1 = -v\,\Delta t(F_1' + \tilde{F}_1)/2. \tag{19}$$

Again assuming complete convergence, Eqs. (11), (13), (18), and (19) yield

$$z^2 + 2vi(1 + \omega_0^2\,\Delta t^2/4)\,z - \omega_0^2 = 0. \tag{20}$$

Solving Eqs. (20) and (15) for $\beta_2 = \mathrm{Re}(\omega)$ and $\Gamma_2 = \mathrm{Im}(\omega)$ yields the relative frequency and growth rate errors for this algorithm:

$$\frac{\beta_2 - \beta}{\beta} = -\frac{\omega_0^2 - v^2}{12}\Delta t^2 - \frac{(\omega_0^2 - v^2)^2}{120}\Delta t^4 + O(\Delta t^6), \tag{21}$$

$$\frac{\Gamma_2 - \Gamma}{\Gamma} = \frac{v^2}{3}\Delta t^2 - \frac{5(\omega_0^2 - v^2)^2}{48}\Delta t^4 + O(\Delta t^6). \tag{22}$$

Since $\omega_0 \gg v$, the split-step algorithm is seen to give a significantly more accurate collisional damping rate and only a slightly less accurate oscillation frequency than the single-step algorithm.

3. *Convergence of Iteration*

The convergence condition for the iterated first half-step in the split-step algorithm is found by writing Eqs. (11), (13), and (18) after $q-1$ iterations, to examine the $q$th iteration:

$$F_0^q - F_0 = -ik_l \Delta t(F_1^q + F_1)/6, \tag{23}$$

$$F_1^q - F_1 = -ik_l \Delta t(F_0^q + F_0 - \varphi^{q-1} - \varphi)/2, \tag{24}$$

$$\varphi^q - \varphi = i\frac{\omega_h^2 \Delta t}{2k_l}(F_1^q + F_1). \tag{25}$$

Solving Eqs. (23) and (24) for $F_1^q$ and substituting the result into Eq. (25) yields

$$\varphi^q = \psi - \delta^2 \varphi^{q-1} = \psi \sum_{q'=0}^{q-1} (-\delta^2)^{q'} + (-\delta^2)^q \varphi, \tag{26}$$

where $\psi$ consists of terms which do not vary during the iteration and $\delta = (\omega_h \Delta t/2)(1 + k_l^2 \Delta t^2/12)^{-1/2} \simeq \omega_h \Delta t/2$ for $k_l \Delta t \ll 1$. It follows from Eq. (26) that a necessary condition on $\Delta t$ for the iteration to converge is that $\delta < 1$.

4. *Numerical Stability*

The computations are carried out with a specified number, $Q$, of iterations at each time-step and the error due to incomplete convergence can be expressed from Eq. (26) as

$$\Delta^Q \simeq \varphi^{Q+1} - \varphi^Q = 2(-\delta^2)^{Q+1}\left[\varphi - F_0 - i\frac{2}{k_l \Delta t}F_1\right]. \tag{27}$$

Writing Eqs. (23) through (25) for the $Q$th iteration ($q = Q$) with $\varphi^{Q-1} = \varphi^Q - \Delta^{Q-1}$; setting the new values $F_0'$, $F_1'$, and $\varphi'$ equal to $F_0^Q$, $F_1^Q$, and $\varphi^Q$; and assuming a time dependence of the form $\exp(-i\omega t)$ yield the dispersion relation

$$\left(\frac{\xi - 1}{\xi + 1}\right)^2 = -\frac{\omega_0^2 \Delta t^2}{4}[1 - (-\delta^2)^Q] - (-\delta^2)^Q\left(\frac{\xi - 1}{\xi + 1}\right), \tag{28}$$

where $\xi = \exp(-i\omega \Delta t)$. For $\omega \Delta t \ll 1$, $\xi \simeq 1 - i\omega \Delta t$ and Eq. (28) yields the growth rate

$$\Gamma_Q = -\frac{(-\delta^2)^Q}{\Delta t}. \tag{29}$$

Thus for an even number of iterations (e.g., $Q = 2$ or 4), incomplete convergence leads to damping, while for an odd number of iterations (e.g., $Q = 3$), incomplete convergence gives a numerical instability that can easily dominate the simulation results.

## V. Examples

The code implementing the present algorithm has been used extensively in computer studies of the dissipative trapped-electron instability and of curvature and gradient drift effects on trapped-electron modes; these results are presented elsewhere [6]. The computations presented next are instead chosen to answer questions of numerical convergence and accuracy.

### 1. *Trapping of Unperturbed Electrons*

A primary concern in the present simulations is the number of poloidal sidebands, $l_{max}$, required on each side of the central mode to resolve trapping phenomena adequately. This question is first examined here by considering unperturbed electron motions; magnetic curvature and gradient drifts are neglected. In this case, there is no wave, Eq. (2) drops out, and the distribution function is obtained from Eq. (1) with $\varphi = 0$, $m = 0$, $k_\| = 0$, and $\rho_e/r = 0$. In order to observe trapping oscillations without the phase-mixing effects due to the energy dependence of the bounce frequency, a monoenergetic initial distribution function with $v = 1$ is chosen. This initial distribution function is independent of the poloidal angle $\theta$ but is given a pitch-angle dependence of the form $1 - \cos\alpha$, from which $f_{l=0} = (1-u)\,\delta(v-1)/4\pi$ and $f_{l\neq 0} = 0$ at $t = 0$.

The time dependence of the mean parallel velocity $\langle v_\| \rangle_0$ is shown in Fig. 4 for $\varepsilon = 0.2$, $\nu = 2 \times 10^{-4}$, and $l_{max} = 1, 4$, and 10. These computations were carried out with $\Delta u = 1/29$, $\Delta t = 0.05$, and $Q = 2$ iterations. Note that $\langle v_\| \rangle_0 = -1/3$ at $t = 0$, as a result of the initial $1 - u$ dependence of the distribution function, and that for $t > 0$ it proceeds to oscillate with a period $\simeq 24$. The theoretical expression for the bounce

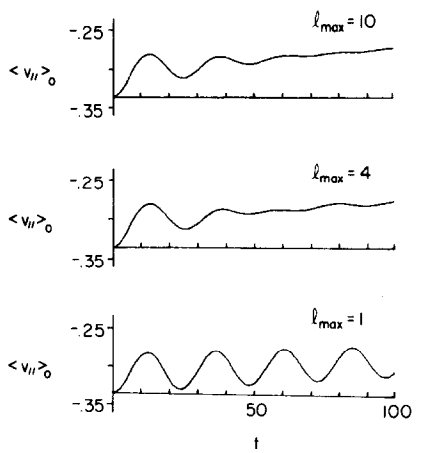


FIG. 4. Averaged electron parallel velocity, $\langle v_\|(t) \rangle$, shows trapping oscillations at the bounce frequency $\omega_b = \varepsilon^{1/2} 2^{-3/4}$ in normalized time units, with $\varepsilon = 0.2$. More poloidal sidebands than $l_{max} = 4$ does not impove resolution of trapping effects on $\langle v_\| \rangle$. Effect of collisions ($\nu = 0.0002$) causes $|\langle v_\| \rangle|$ to decay.

frequency, in normalized units, is [5] $\omega_b = \varepsilon^{1/2} v / 2^{3/4}$. This gives in the present case a trapping period $t_b = 2\pi/\omega_b = 23.63$, which agrees closely with the results of Fig. 4. For $l_{max} = 1$, i.e., using only three poloidal modes, the trapping oscillations persist, but when a larger number of modes is retained, $l_{max} = 4$ and 10, the oscillations damp rapidly after the first period. This damping is caused by phase mixing resulting from the dependence of bounce frequency on the amplitude of the trapping oscillations. These results are similar to results reported earlier [5] except that now collisional pitch-angle diffusion has been included, causing the value of $\langle v_\parallel \rangle_0$, when averaged over several trapping periods, to decay slowly in time. For $l_{max} = 1$, the rate of decay is very close to the collision frequency $\nu = 2 \times 10^{-4}$, while for $l_{max} = 4$ and 10, somewhat larger decay rates are apparent.

The pitch-angle dependence of the distribution function $f_0$, averaged over $\theta$, is shown in Fig. 5 for the three cases $l_{max} = 1, 4$, and 10. At $t = 15$, which corresponds approximately to a half trapping period, a large variation from the initial distribution occurs in the region $|u| \lesssim 0.45$, which corresponds to trapped electrons. At $t = 25$, which corresponds to a complete trapping period, the curves have returned close to their initial shapes. Contour plots of $f(\theta, u)$ at $t = 25$ are also given in Fig. 5. For $l_{max} = 4$ and 10, these plots clearly show the trapping region in the form of a vortex.

These computations show that, while trapping effects are indeed recovered using

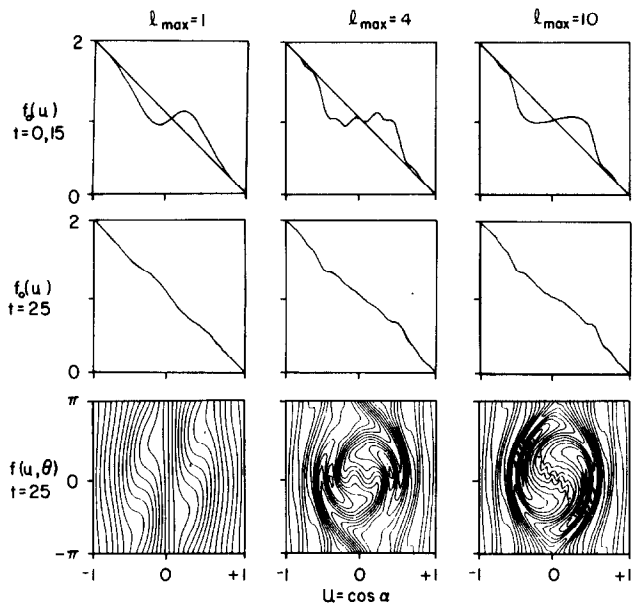


FIG. 5. Pitch-angle distribution averaged over poloidal angle $\theta$, for same runs as in Fig. 4. Top row: Initially ($t = 0$) and after roughly $\frac{1}{2}$ bounce period ($t = 15$) to show greatest departure from initial shape. Middle row: After almost one bounce period ($t = 25$) the averaged distribution has returned almost to initial condition. Lower row: Contour plots in $(u, \theta)$ plane clearly show trapping region for $l_{max} = 4$ and 10.

only $l_{max} = 1$, the resolution of the fine structure of the distribution function resulting from trapping oscillations requires a larger number of modes. Since this fine structure is smeared out by collisional diffusion, the number of modes required depends on the collision frequency. For the case considered here ($\varepsilon = 0.2$, $\nu = 2 \times 10^{-4}$) values of $l_{max}$ between 4 and 10 appear sufficient.

## 2. *Drift Waves*

The accuracy of the algorithm to represent drift wave oscillations is examined by setting $\varepsilon = 0$ to exclude trapping effects. In this case no coupling occurs between poloidal modes and we may set $l_{max} = 0$. Three simulations were done with $v_D = 2 \times 10^{-4}$, $\lambda_D = 2 \times 10^{-3}$, $\eta = 1$, $m = 10$, $\gamma = 0.1$, $k_\parallel = 0.1$, and constant collision frequencies, $\nu = 10^{-3}$, $10^{-2}$ and $2 \times 10^{-2}$. These computations were carried out with $\Delta u = 1/14$, $\Delta t = 0.1$, and $Q = 2$ iterations. A Maxwellian distribution function was considered with $v_{max} = 4$ and $\Delta v = 1/14$.

The resulting simulation potential is plotted as a function of time in Fig. 6 for the three cases. The high-frequency oscillations are evident in these plots. For this case, the expected high-frequency $\beta = k_\parallel \gamma / m\lambda_D = 0.5$, gives a period $2\pi/\beta = 12.6$, which is close to the period observed (12.2) in Fig. 6. The high-frequency oscillations have an amplitude modulation, which is the result of beating between two high-frequencies having a difference of the order of the drift frequency $\omega_*$. Collisions cause a damping

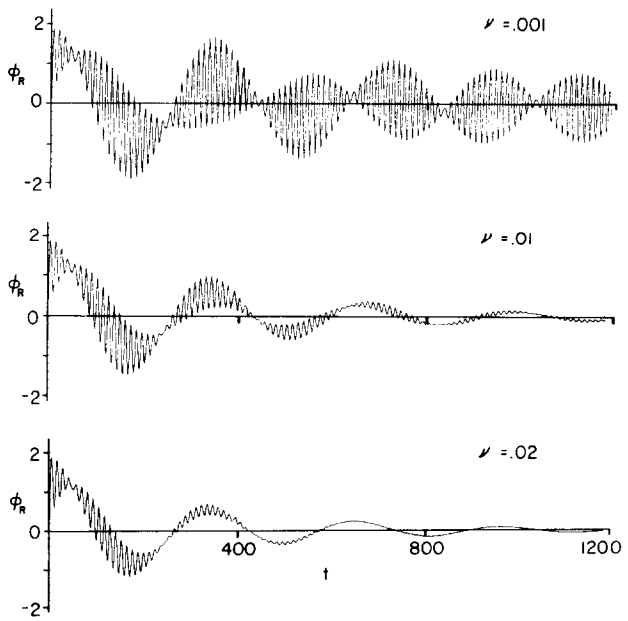


FIG. 6. Simulation results for real part of electric potential $\varphi_R(t)$, using a Maxwellian distribution. Trapping effects have been dropped ($\varepsilon = 0$). Both low-frequency drift wave and high-frequency oscillations are evident.

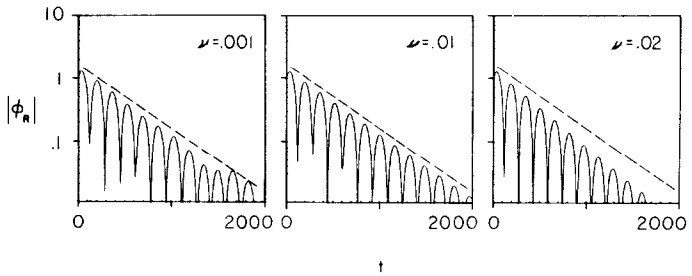


FIG. 7. Electric potentials for same runs as in Fig. 6, after filtering out high frequency. The dashed lines indicate the predicted collisionless Landau damping rate for this case ($\eta = 1$).

of the high-frequency oscillations at the rate $\Gamma = -\nu$, which gives decay by a factor $1/e \simeq 0.37$ in times 1000, 100, and 50, respectively, for the three cases considered. This damping is difficult to measure accurately on the plots of Fig. 6, because of the beating of the high-frequency oscillations, but the trend toward increased damping with increasing collision frequency is evident.

Low-frequency oscillations related to the drift wave are also observed in Fig. 6, but are more clearly displayed in Fig. 7, where the potential has been averaged over the high-frequency period and is now plotted on a logarithmic scale. For this case, the theoretical drift frequency $\omega_* = mv_D/\gamma = 2 \times 10^{-2}$ must be modified by a small correction [5], $\delta\omega = -\omega_*(m\lambda_D/\gamma)^2$, due to finite $\lambda_D$. Thus the expected drift wave frequency is $\omega = 1.92 \times 10^{-2}$, corresponding to a period $2\pi/\omega = 327$, which is very close to the periodicity (320) observed in Fig. 7. With $\eta = 1$, the drift wave is also affected by Landau damping at the theoretical rate $\Gamma_L = -0.0023$, which is indicated by the broken lines in Fig. 7. For $\nu = 10^{-3}$ and $10^{-2}$, the drift wave follows the Landau damping rate closely; thus collisions are observed to affect the low-frequency damping rate significantly only for $\nu \gtrsim 2 \times 10^{-2} \simeq \omega_*$.

The low-collision case, $\nu = 10^{-3}$, shows an irregularity in amplitude near $t = 1500$. This irregularity becomes stronger in the collisionless case ($\nu = 0$) and is thought to be a recurrence phenomenon related to the discrete representation of the distribution function in $u$ and $v$. Note that, for a monoenergetic distribution the recurrence time [8], due to the discrete representation of parallel velocities with separation $\Delta v_\parallel = v\,\Delta u$, is $\tau_r = 2\pi/(k_\parallel \Delta v_\parallel) = 880/v$ (here $k_\parallel = 0.1$ and $\Delta u = 1/14$). For the Maxwellian distribution considered here, the recurrence times for different energies are different. This results in a smearing of the recurrence, and this effect is indeed reduced when a finer mesh in the representation of the distribution function in $u$ and $v$ is used. Since the code is normally used with collision frequencies $\nu \gtrsim 10^{-3}$, this recurrence effect does not seem to be an important limitation.

### 3. *Numerical Stability*

Several computations were done to verify the high-frequency numerical stability results of Section IV-4. In these computations, we set $\varepsilon = 0$, $\nu = 0$, and $v_D = 0$ to eliminate trapping and collisional effects and low-frequency oscillations. A single

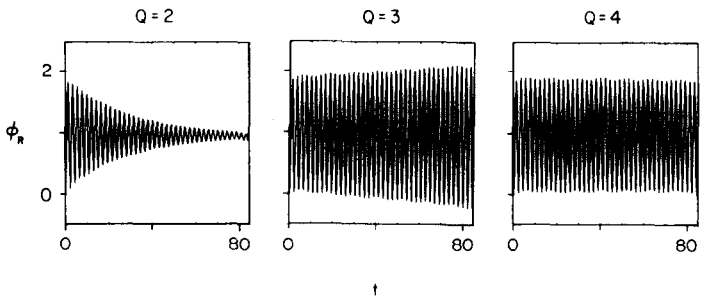


FIG. 8. High-frequency, finite-iteration instabilities for two, three, and four iterations per time-step.

mode is considered ($l_{max} = 0$) with $m = 10$, $\gamma = 0.1$, $\lambda_D = 2 \times 10^{-3}$, $\Delta u = 1/14$ and a monoenergetic distribution $f_0 = \delta(v - 1)/4\pi$ is used.

For the case shown in Fig. 8, $k_\parallel = 1.$ and $\Delta t = 0.2$. The analysis of Section IV gives $\omega_h = 2.89$ and $\delta = 0.2888$. With $Q = 2, 3,$ and 4 iterations every time-step, the theoretical growth rates are, respectively, $\Gamma_2 = -0.0347$ (stable), $\Gamma_3 = 0.0029$ (unstable), and $\Gamma_4 = -0.00024$ (stable). These results agree closely with the computation results of Fig. 8. Here damping is observed for $Q = 2$, with a measured growth rate of $-0.038$; growth is observed for $Q = 3$, with a measured growth rate of 0.003; and no measurable growth or damping occurs for $Q = 4$. Other computations with a variety of values of $k_\parallel$, $\Delta t$, and $Q$ confirm these results. For example, for other simulations having $k_\parallel = 2$ and $\Delta t = 0.1$, the theoretical growth rates are $\Gamma_2 = -0.069$, $\Gamma_3 = 0.0058$, and $\Gamma_4 = -0.00048$, while the corresponding measured values are $-0.067$, 0.0054, and $-0.00058$.

4. *Accuracy Tests*

To consider the code's numerical accuracy in finding the physical growth rate of a trapped-electron instability, a series of simulations was done involving curvature and gradient drift resonance. The physical parameters chosen for these runs are $v_D = 2 \times 10^{-4}$, $m = 10$, $\gamma = 0.1$ (so that $\omega_* = 0.02$), $\lambda_D = 2 \times 10^{-3}$, $\eta = 1$, $k_\parallel = 0.1$, $\nu = 10^{-3}$, and $\rho_e/r = 7 \times 10^{-4}$. A Maxwellian electron distribution was used with a velocity space grid having $v_{max} = 4$, $\Delta v = 1/14$, and $\Delta u = 1/14$. The numerical parameters that were varied in these runs were time-step size $\Delta t$, iteration number $Q$, and the number of poloidal modes $l_{max}$ on each side of the central (rational) mode. The normalized drift wave growth rates, $\Gamma/\omega_*$, obtained from these simulations, are presented in Table I to illustrate the effects of these numerical parameters on accuracy of the simulations.

According to the analysis of Section IV, simuations using an odd number of iterations should exhibit a high-frequency numerical instability due to incomplete convergence. Since the highest poloidal mode ($l = l_{max}$) involves the highest frequency ($\omega_h = (k_\parallel + l)\,\gamma/m\lambda_D$), the largest and earliest high-frequency growth should appear there. As simulation time elapses, these high frequencies should couple due to trapping, downward to the other poloidal modes until the simulation yields growing

TABLE I

Observed Normalized Growth Rate $\Gamma/\omega_*$ of low-frequency drift wave potentials[a]

| $l_{max}=$ | 1 | 1 | 1 | 4 | 4 | 10 |
|---|---|---|---|---|---|---|
| $\Delta t=$ | 0.1 | 0.125 | 0.15 | 0.025 | 0.05 | 0.02 |
| $Q=2$ | 0.255 | NI | NI | 0.155 | 0.155 | 0.148 |
| $Q=3$ | NI (0.255) | NI | NI | NI (0.155) | NI | NI |
| $Q=4$ | 0.255 | 0.255 | 0.255 | 0.155 | 0.155 | 0.148 |

[a] Growth is due to curvature and gradient drift resonances [7]. For the same $l_{max}$, rates are consistent with each other whenever high-frequency numerical instability (NI) is not present. Choosing $l_{max}$ greater than 4 does not significantly improve accuracy of results.

(numerical instability) high frequencies alone and the drift-wave results (physical instability) are lost.

Table I shows that while such numerical instability (NI) behavior is indeed observed in all the $Q=3$ runs, the drift-wave growth rates are nevertheless retrievable in a few cases as indicated. In the $\Delta t=0.1$ case ($l_{max}=1$), the drift wave actually grows at a faster rate ($\Gamma/\omega_*=0.255$) than does the high frequency ($\Gamma_{Q=3}(l=1)/\omega_*=0.216$) and is therefore unaffected by the numerical instability. In the $\Delta t=0.025$ case ($l_{max}=4$), even though $\Gamma_{Q=3}(l=4)/\omega_*=0.57$ is larger than the drift wave's growth rate, the time it takes for this growing high frequency to couple down from $l=l_{max}=4$ to the central mode ($l=0$) is long enough that a good measurement of the physical growth rate is possible before the low-frequency drift wave is finally overtaken by the high-frequency numerical instability.

Such high-frequency instabilities are seen to be quenched as predicted earlier by using an even number of iterations $Q=4$. The $Q=2$ numerical instabilities indicated in Table I are not high frequency: they appear simultaneously in all modes instead of first at $l_{max}$ and then coupling down to other modes. Using $Q\geqslant 4$ iterations for the same parameters effectively quenches this instability too and suggests therefore that these represent a convergence problem.

Two more important conclusions are to be drawn from Table I. First, when numerically stable drift-wave results are obtained from the simulation code, they show no dependence on simulation parameters $\Delta t$ and $Q$. Second, while having only one poloidal sideband ($l_{max}=1$) is apparently sufficient to recover the presence of the curvature drift resonance instability, an accurate computation of this instability's growth rate requires better resolution of the trapped electron motions and therefore must involve $l_{max}\gtrsim 4$.

## VI. Conclusions

In the numerical algorithm presented in this paper for solving the drift-kinetic equation in toroidal geometry, Fourier transforms with respect to the poloidal and

toroidal angles were used, and a split timestep was introduced in which the collisionless and collisional parts of the drift-kinetic equation are calculated separately. The analytical developments and numerical tests of Section IV and V have shown several important properties of this algorithm.

(1) The split time-step was shown to be both simpler and more accurate than a single step, as long as $\nu \ll \omega_h$, where $\nu$ is the collision frequency and $\omega_h$ is the high electron oscillation frequency. This condition is always satisfied in simulations of drift and trapped-electron modes.

(2) The time-step $\Delta t$ is limited by the high frequency $\omega_h$, and must satisfy the necessary condition $\delta = \omega_h \Delta t/2 < 1$ for convergence of the iteration. The solution is numerically stable when an even number of iterations, $Q$, is used and is unstable when $Q$ is odd, with growth rates given by Eq. (29).

(3) Numerical tests show that resonant particle effects giving Landau damping (or excitation) of drift waves are correctly represented, and that recurrence problems related to discrete representations of velocity space with finite intervals $\Delta u$, $\Delta v$ are not serious for collision frequencies $\nu \gtrsim \Gamma_L$, where $\Gamma_L$ is the Landau damping (or excitation) rate.

(4) The number of poloidal modes necessary to represent electron trapping and associated trapped-electron modes depends on the required accuracy and on the collision frequency. The basic trapped-electron effects are obtained with three modes only ($l_{max} = 1$) and numerical test shows that for $\nu \gtrsim 10^{-2}\omega_b$ ($\omega_b$ is the bounce frequency) the poloidal Fourier expansion converges satisfactorily with nine modes ($l_{max} = 4$).

This algorithm is applicable to linearized computer simulations of trapped-electron modes in tokamaks in the local approximation. The algorithm deals primarily with the electrons; the ions have been treated here only in terms of their electric drift ($\omega_* \ll \Omega_i$). More complete ion models, including ion Landau damping (or excitation) and finite gyroradius corrections could readily be introduced in the algorithm. A generalization to nonlinear solutions would involve toroidal mode coupling and therefore would require additionally considering a set $(n \pm l)$ of toroidal modes. For a limited number of toroidal and poloidal modes (e.g., five to nine modes of each type) such a generalization appears to be feasible.

Finally, a generalization to non-local simulations would of course be of considerable interest for examining radial eigenmodes and shear stabilization of trapped-electron modes. This requires the introduction of a radial grid and the computing times of $\sim 8$ min CRAY $-$ 1 in the present code would be approximately multiplied by the number of radial grid points. To make some progress in non-local computations, a non-local code has recently been written using Eq. (1) for the electrons and including gyrokinetic ions (i.e., including finite ion gyroradius corrections), but operating in the frequency rather than in the time domain. This non-local code will soon allow us to examine shear stabilization of trapped-electron modes and to estimate the number of radial grid points which would be required by a large-scale time-domain simulation code.

## APPENDIX: APPLICATION OF THE CHARGE NEUTRALITY CONDITION

The Poisson equation is used in the algorithm presented in this paper to compute the potential. As we have seen in Section IV, this yields oscillations at the frequency $\omega_h = k_\parallel \gamma / m\lambda_D$. An alternate method would seem to be the application of the charge neutrality condition, which would eliminate the need to introduce the Debye length into the problem. However, we show in this Appendix that, in the present case, this approach would not eliminate high-frequency oscillations, but would on the contrary introduce non-physical oscillations at an even higher frequency[1].

The charge neutrality condition may be derived from Eq. (2) by setting $\lambda_D = 0$;

$$\varphi_{m+l} = \frac{\gamma}{k_\parallel v_D} \left\{ (k_\parallel + l)\langle v_\parallel \rangle_{m+l} - \frac{\varepsilon}{2} (\langle v_\parallel \rangle_{m+m+1} - \langle v_\parallel \rangle_{m+l-1}) \right.$$
$$+ \frac{1}{\gamma} \frac{\varepsilon \rho_e}{r} [(m + l + 1)(p_{m+l+1} - \varphi_{m+l+1})$$
$$\left. + (m + l - 1)(p_{m+l-1} - \varphi_{m+l-1})] \right\}. \tag{A1}$$

Setting $\varepsilon = 0$ to exclude trapping effects, expanding the distribution function in Legendre polynomials in the manner of Section IV, and assuming $l = 0$, $\eta = 0$, and $\nu = 0$, Eq. (1) yields

$$\dot{F}_0 = -i \frac{k_\parallel}{3} F_1 + i \frac{v_D}{\gamma} (m - k_\parallel)\varphi, \tag{A2}$$

$$\dot{F}_1 = -ik_\parallel (F_0 - \varphi) \tag{A3}$$

and Eq. (A1) gives

$$\varphi = \frac{\gamma}{3v_D} F_1. \tag{A4}$$

This set of equation yields the dispersion relation

$$\omega \left( 3\omega + \frac{k_\parallel \gamma}{v_D} \right) + (m - 2k_\parallel) k_\parallel = 0. \tag{A5}$$

For $v_D^2 \ll \gamma k_\parallel / 12m$ this reduces to $\omega = -k_\parallel \gamma / 3v_D$. In the example considered in part (3) of Section V but using $k_\parallel = 0.1$ and $v_D = 2 \times 10^{-4}$, we find $\omega = -16.7$. This is a factor of 58 larger than the high frequency ($\omega_r = 0.29$) obtained with $\lambda_D = 2 \times 10^{-3}$

[1] This high frequency disappears when the ion model includes inertia.

## ACKNOWLEDGMENTS

This work was supported by the Department of Energy under Contract EY-76-S-02.2200. Acknowledgment is made to the National Magnetic Fusion Energy Computing Center for computer time used in this research.

## REFERENCES

1. B. B. KADOMTSEV AND O. P. POGUTSE, *Zh. Eksp. Teor. Fiz.* **51** (1966), 1734. [*Sov. Phys. JETP* **24** (1967) 1172.]
2. B. B. KADOMTSEV AN O. P. POGUTSE, *Dokl. Akad. Nauk. SSSR* **186** (1969), 533. [*Sov. Phys. Dokl.* **14** (1969), 470.]
3. W. M. MANHEIMER, "An Introduction to Trapped-Particle Instability in Tokamaks" TID27157, Technical Information Center, ERDA, 1977.
4. R. D. HAZELTINE, *Plasma Phys.* **15** (1973), 77.
5. J. DENAVIT AND C. E. RATHMANN, *Phys. Fluids* **21** (1978), 1533.
6. T. L. CRYSTAL AND J. DENAVIT, *Phys. Fluids*, in press.
7. J. C. ADAM, W. M. TANG, AND P. H. RUTHERFORD, *Phys. Fluids* **19** (1976), 561.
8. J. DENAVIT, *J. Comput. Phys.* **9** (1972), 75.